International Journal of Technology 14(7) 1527-1536 (2023)
Received July 2023 / Revised September 2023 / Accepted November 2023

International Journal of Technology

http://ijtech.eng.ui.ac.id

Detection of Low Hydrostatic Pressure Using Fiber Bragg Grating Sensor

Naufal Aiman Madani[1], Retno Wigajatri Purnamaningsih[1*], Nji Raden Poespawati[1], Maratul Hamidah[2], Sasono Rahardjo[2], Dena Karunianto Wibowo[3]

[1]*Optoelectronics Laboratory, Department of Electrical Engineering, Universitas Indonesia, Depok 16425, West Java, Indonesia*
[2]*Research Center for Electronics, National Research and Innovation Agency, South Tangerang 15314, Banten, Indonesia*
[3]*Department of Applied Physics, KTH Royal Institute of Technology, SE-100 44 Stockholm, Sweden*

Abstract. The aim of this study was to investigate the detection of low hydrostatic pressure, serving as the foundation for developing an underwater pressure sensor. This included creating a single-mode, uniformly structured Fiber Bragg Grating (FBG) with a stainless-steel coating. The experiment included loading the sensor with different volumes of fresh water ranging from 0 ml to 6 ml, in increments of 0.25 ml, in the perpendicular vertical direction. This volume range corresponded to hydrostatic pressures ranging from 0 Pa to 40.55 Pa. The experimental results showed a consistent linear relationship between low hydrostatic pressure and Bragg wavelength, implying a sensitivity of 0.8092 pm/Pa, according to theoretical expectations. Subsequently, mathematical simulations were conducted based on the results to predict the sensor performance under various potential seabed temperatures. The simulation results indicated that as the temperature rose, there was a corresponding increase in the reflected wavelength difference by $\mathbf{5.3754} \times \mathbf{10^{-9}}$ nm/Pa for every 1°C increase in seawater temperature.

Keywords: Bragg wavelength; Fiber bragg grating; Low hydrostatic pressure

1. Introduction

Pressure is a crucial parameter in analyzing environmental conditions and has diverse applications, which include underwater environmental monitoring (Matsumoto *et al.*, 2018), as well as earthquake and tsunami detection (Tanioka, 2018). Underwater pressure measurements typically comprise the use of a Bottom Pressure Recorder (BPR) system and a buoy (Irfan *et al.*, 2021). BPR is deployed in the Ocean Bottom Unit (OBU) module designed to detect underwater pressure and transmit the collected data to a buoy. Subsequently, data from both OBU and buoy are sent to a ground station for further analysis (Winarno *et al.*, 2021; Suastika *et al.*, 2019).

The use of OBU and buoy for underwater pressure detection presents certain limitations. These limitations include limitations to near real-time monitoring capability and high production, operational, and maintenance costs. The identified shortcomings of buoy-based pressure detection techniques have prompted study efforts and the implementation of fiber optic-based sensors for underwater measurements (Yang, Zhu, and An., 2022; Ramirez *et al.*, 2022; Lei, 2020).

*Corresponding author's email: retno.wigajatri@ui.ac.id, Tel.: +62-21-7270078
doi: 10.14716/ijtech.v14i7.6714

Fiber optic sensors offer several advantages, such as applicability in hard-to-reach locations and higher immunity to electromagnetic interference (EMI) (Rong and Qiao, 2019). These advantages, among others, drive numerous developments in optical-based sensors, including accelerometers (Zhang *et al.,* 2017), which find applications in various electronics and diverse fields (Zainudin *et al.,* 2017; Dwiyantoro, Nugraha, and Choi, 2016).

An essential aspect of underwater measurements includes detecting pressure changes developing from the movement of objects around the sensor (Nishida *et al.,* 2018). In addition, it is crucial to understand the sensor threshold, resolution, and sensitivity. Numerous studies explored hydrostatic pressure in water. (Her and Weng, 2021) developed a Fiber Bragg Grating (FBG) sensor with an integrated epoxy diaphragm for measuring water pressure and depth. The study showed sensitivities ranging from 175.5 pm/kPa to 43.7 pm/kPa for FBG in the pressure range of 491 – 2943 Pa. In another study, (Bhowmik *et al.,* 2015) investigated the sensitivity of hydrostatic pressure on polymer-type FBG with different diameters to assess the impact of etching on sensitivity. The results showed that pressure in the range of 0-1000 kPa, increasing by 100 kPa, led to a sensitivity of 0.2 pm/kPa for unetched FBG and 0.75 pm/kPa for etched FBG. Additionally, (Nguyen, Chiang, and Tsai, 2022) examined a bare FBG pressure sensor based on an oval-shaped 3D-printed structure. In the range of 0 - 0.45 MPa, with increments of 0.05 MPa, a sensitivity of 6.834 nm/MPa was observed. Furthermore, (Amos, Prabhu, and Nuguna, 2017) proposed a theoretical design of a hybrid FBG/EFPI sensor for temperature and pressure measurements in subsea underwater applications. Simulations showed an increase in temperature sensitivity from 13.95 pm/°C to 23.89 pm/°C.

There was no recent experiment performed with stainless steel-coated FBG pressure sensors to detect small changes in water pressure, particularly under 50 Pa. In this study, experiments were conducted within the range of 0 to 40.55 Pa, with an increase of 1.69 Pa. The aim was to observe the performance of a stainless steel-coated, uniform-structured, and single-mode Fiber Bragg Grating (FBG) pressure sensor in detecting very low hydrostatic pressure. Furthermore, based on the results, mathematical simulations were conducted to predict the sensor performance in detecting subtle pressure changes as experienced while immersed in underwater conditions. In Section 2, the operational concept of FBG is explained and the experimental setup and procedures are described in Section 3. Results and predictions of sensor output in the form of mathematical simulations are described in Section 4, while Section 5 contains the conclusions. It is crucial to be aware that all experiments were carried out at the Optoelectronics Laboratory, Electronics Research Center (PRE) of the National Research and Innovation Agency (BRIN). Consequently, the results are expected to be the basis for the development of underwater pressure sensors in Indonesia.

2. Literature Review

2.1. Operating Principle of Fiber Bragg Grating (FBG)

FBG functions by selectively filtering specific wavelengths of light through partial reflection and transmission. This mechanism relies on tracking the reflected Bragg wavelength (Werneck, Allil, and Nazare, 2017). When light enters, only the one that matches the FBG Bragg wavelength will be reflected and the rest will pass through to the output. This can be called the resonant condition of a grating which is expressed as follows (Singh *et al.,* 2023).

$$\lambda_B = 2\, n_{eff} \Lambda \tag{1}$$

Where λ_B signifies FBG Bragg wavelength, n_{eff} signifies the effective refractive index of the core, and Λ signifies the grating period.

2.2. Fiber Bragg Grating (FBG) as a Pressure Sensor

Equation (1) clearly shows that Bragg wavelength, maximally reflected, is particularly influenced by the effective refractive index of the fiber core and the grating period. FBG shows heightened sensitivity to changes in both strain and temperature. The effects of strain and temperature on FBG Bragg wavelength are described as follows (Zhang, Tian, and Fu 2017).

$$\frac{\partial\lambda_B}{\partial T\partial\varepsilon} = \frac{\partial\lambda_B}{\partial T}\Delta T + \frac{\partial\lambda_B}{\partial\varepsilon}\Delta\varepsilon \tag{2}$$

In Equation (2), ΔT represents the change in temperature, and represents the change in strain.

The strain change in Equation (2) arises from two sources: mechanical strain (ε_m) and temperature strain (ε_T). The relationship between these two strains is defined as follows (Tanguy, Li, and Mengxi, 2021).

$$\varepsilon = \varepsilon_m + \varepsilon_T \tag{3}$$

Temperature strain (ε_T) is defined as the product of the material coefficient of thermal expansion (α_{SP}) and the change in temperature (ΔT), as expressed by (Leal-Junior *et al.*, 2019).

$$\varepsilon_T = \alpha_{sp} \,.\, \Delta T \tag{4}$$

By substituting the value of ε_T from Equation (4) into Equation (3), we can further derive Equation (2) to determine the shift in Bragg wavelength rising from the impact of strain and temperature changes, as outlined by (Yang *et al.*, 2019).

$$\Delta\lambda_B = [(1 - p_e)(\varepsilon_m + \varepsilon_T) + (\alpha_{\delta T})\Delta T]\lambda_B$$

$$\Delta\lambda_B = \left[(1 - p_e)(\varepsilon_m + \alpha_{sp}.\Delta T) + (\alpha_{\delta T})\Delta T\right]\lambda_B \tag{5}$$

In this context, p_e denotes the photo-elastic coefficient, ε signifies the total strain arising from both mechanical strain (ε_m) and temperature strain (ε_T), $\alpha_{\delta T}$ represents the change in the refractive index due to temperature, and $\Delta\lambda_B$ denotes the change in Bragg wavelength.

If FBG is used as a pressure sensor on an object experiencing no temperature changes, the temperature change value can be considered zero ($\Delta T = 0$) (Her and Weng, 2021). Consequently, Equation (5) can be streamlined to Equation (6), as outlined by (Kumar, Sharan and Sreerangaraju, 2021).

$$\Delta\lambda_B = \lambda_B(1 - p_e)\varepsilon \tag{6}$$

3. Experimental Setup

Figure 1 showed the schematic setup of the Bragg wavelength measurement system, designed to simulate hydrostatic pressure through varying water volume conditions. In the schematic setup shown in Figure 1, a light source, represented by SLED DL-BP1-1501A with a wavelength range of 1535 - 1565 nm, was connected to a 3-port circulator for directing light. The light wave entered through port 1 and exited at port 2, directed toward the stainless steel-coated single-mode uniform FBG positioned on the measurement object. The reflected light wave from FBG re-entered the circulator through port 2 and exited at port 3, directed toward the optical interrogator. Port 3 lacked an input circulator, making it an optical null. The central reflected wavelength of the single-mode uniform grating FBG used in the measurement was observed in an optical spectrometer integrated into the software of the optical interrogator I-MON 512 USB.

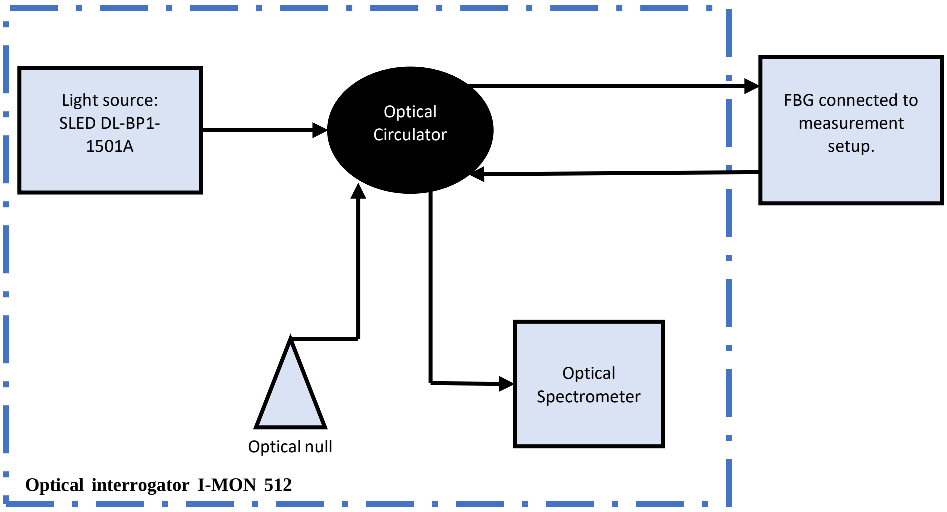

Figure 1 Schematic of FBG sensor setup

The outcome of this test included comparing the central reflected wavelength with the applied pressure on FBG, specifically the pressure exerted by the water introduced into the container. Figure 2 showed a visual representation of the setup used in this experiment.

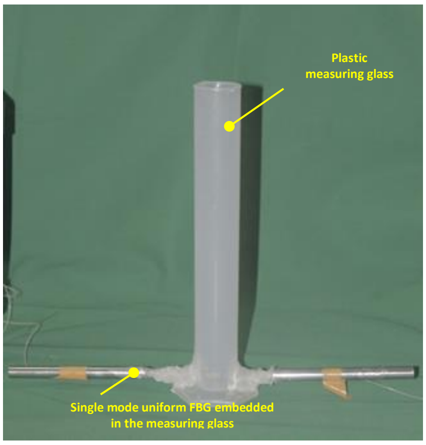

Figure 2 Experimental setup for FBG experiment under low hydrostatic pressure

In the experiment, a stainless steel-coated was placed on a single-mode uniform FBG at the bottom of a plastic measuring glass with a diameter of 4.3 cm. FBG was installed by drilling holes on both sides of the measuring glass bottom, and silicone sealant covered the holes. Subsequently, the experimental setup experienced low hydrostatic pressure by incrementally adding water droplets with a volume of 0.25 ml. Water volume consistency was maintained using a syringe pump into the measuring glass, as shown in Figure 3. The addition of water droplets occurred gradually, ranging from 0 ml to 6 ml with increments of 0.25 ml. Similar to prior tests, data were collected at a frequency of 60 samples per minute or 1 sample per second. The data from the optical spectrum analyzer (OSA) were later averaged per minute to reduce the ripple effect occurring during the initial introduction of water droplets into the measuring glass as seen in Figure 3.

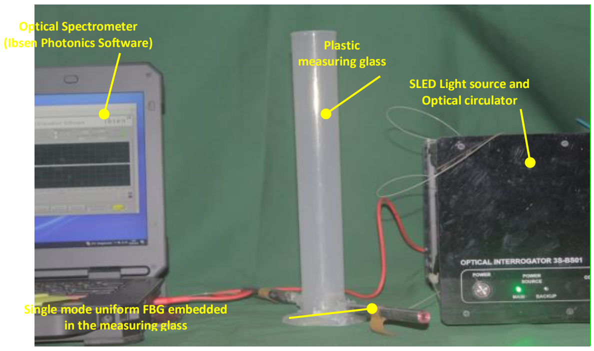

Figure 3 Procedure for conducting an experiment on low hydrostatic pressure using an FBG sensor

Figure 4 showed one of the FBG experiment outcomes under low hydrostatic pressure in the vertical direction. The measurements stabilized when the volume reached 0.75 ml, equivalent to 5.07 Pa of hydrostatic pressure. Below the volume of 0.75 ml, the measurements were unstable due to water pressure from various directions, but this instability was quickly eliminated as the pressure on FBG was mainly from the vertical direction. Another factor that mitigated the effect of water pressure from different directions was the amount of water pressing on FBG at a given time. Selecting a smaller measurement range reduced the ripple that occurred when filling water into the container, thus diminishing the influence of pressure from various directions.

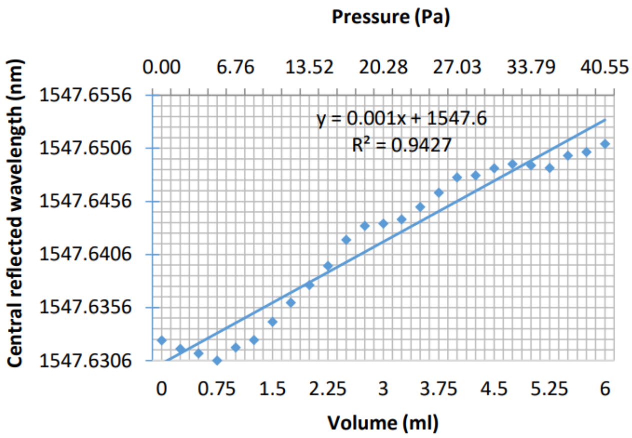

Figure 4 Graph of experimental results for low hydrostatic pressure using FBG sensor at 25°C

4. Result and Discussion

The experiment results, according to Figure 4, showed a threshold point at 0.75 ml, corresponding to a hydrostatic pressure of 5.07 Pa. It was evident from the results that an increase in volume by 0.25 ml, equivalent to a hydrostatic pressure of 1.69 Pa, resulted in a distinguished difference in the reflected wavelength. This difference was particularly visible in the range of 0.75 ml (5.07 Pa hydrostatic pressure) to 4 ml (27.03 Pa hydrostatic pressure), showing a sensitivity of 0.0056 nm/ml or 0.8284 pm/Pa. Figure 5 visually showed the linear range of the experiment.

The established linear relationship signified the consistency of central reflected wavelength changes concerning variations in hydrostatic pressure. The consistency showed that the experiments were affiliated with theoretical expectations. Consequently, further data analysis could be undertaken to predict the sensor performance in underwater environments.

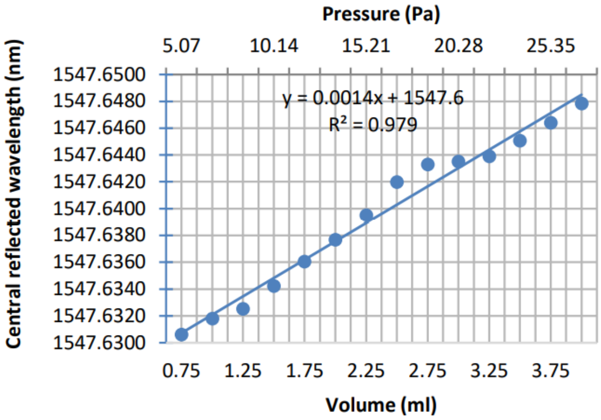

Figure 5 Graph showing the results of the experiment on low hydrostatic pressure using an FBG sensor at 25°C

A theoretical review was conducted to establish the relationship between the applied hydrostatic pressure and the reflected wavelength. In this experiment, silicone sealant was used to install and hold FBG sensor in the cylindrical container. Additionally, Equation (6) could be further derived as outlined by (Her and Weng, 2021).

$$\Delta\lambda_B = \lambda_B(1-p_e)\varepsilon$$
$$\varepsilon = \frac{3P}{8Et^2}(1-v^2)R^2$$
$$\Delta\lambda_B = \lambda_B(1-p_e)\frac{3P}{8Et^2}(1-v^2)R^2 \tag{7}$$
$$P = \frac{\Delta\lambda_B}{\lambda_B}\frac{8Et^2}{3(1-p_e)(1-v^2)R^2}$$

In the given expressions, E denoted Young's modulus, v represented the Poisson's ratio, R signified the radius of the container, t represented the coating thickness, p_e represented the photo-elastic coefficient, and P represented the pressure.

According to Equation (7), an increase in applied pressure on FBG was directly correlated with the rise in Bragg wavelength. In this experiment, FBG was used to measure hydrostatic pressure, which referred to the pressure exerted by fluids. Therefore, Equation (7) could be further derived to ascertain the relationship between the volume of the fluid and FBG Bragg wavelength.

$$P = \rho g h$$
$$\rho g h = \frac{\Delta\lambda_B}{\lambda_B}\frac{8Et^2}{3(1-p_e)(1-v^2)R^2}$$
$$\rho g\frac{V}{\pi R^2} = \frac{\Delta\lambda_B}{\lambda_B}\frac{8Et^2}{3(1-p_e)(1-v^2)R^2}$$
$$V = \frac{\Delta\lambda_B}{\lambda_B}\frac{8Et^2}{3(1-p_e)(1-v^2)}\frac{1}{\rho g}$$
$$\Delta\lambda_B = \frac{\lambda_B\,3\,(1-p_e)(1-v^2)\rho g}{8Et^2}V \tag{8}$$

In this context, g represented the acceleration due to gravity, h denoted the fluid depth, and V represented the fluid volume.

Per Equation (8), it was observed that the increase in Bragg wavelength showed a linear relationship besides volume (V). This arrangement suggested that the conducted measurements were associated with the theoretical foundation. Furthermore, the consistency between theoretical derivation and measurement results implied the ability to predict FBG performance in an underwater environment.

Figure 6 showed the comparison between experimental measurements and calculated results using Equation (8) with $\lambda_B = 1547\, nm$, V ranging from 0.75 ml to 4 ml, $\rho = 1000\, kg/m^3$, $p_e = 0.22$, $v = 0.5$, $g = 9.8\, m/s^2$, $E = 2.03\, MPa$, and $t = 10\, mm$.

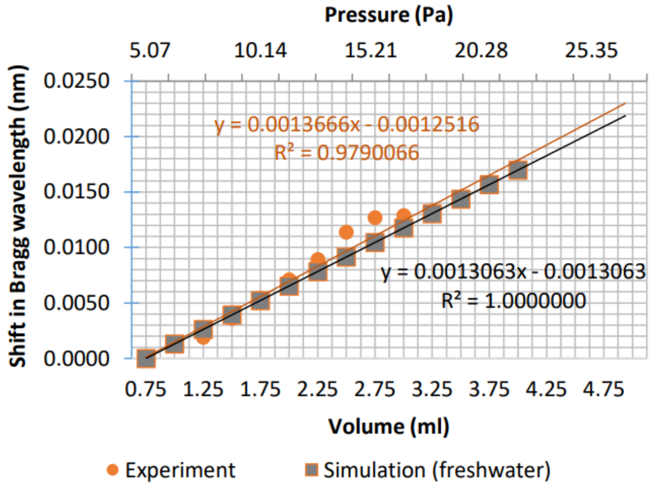

Figure 6 Graph compared the low hydrostatic pressure experiment with its mathematical simulation

The data showed a direct proportionality between the increase in Bragg wavelength and the volume of fresh water. The sensitivity, calculated theoretically, was set upright at 1.3063 pm/0.25 ml or 0.7734 pm/Pa, while the experimental measurements yielded a sensitivity of 1.3667 pm/0.25 ml or 0.8092 pm/Pa. The mean error between experimental and theoretical calculations was 4.6%. The result was comparable to those (Her and Weng, 2021) where sensitivity values around 0.1755 pm/Pa were obtained for measurements ranging from 491 to 2943 Pa. In addition, there was an increase in sensitivity from 0.1755 pm/Pa to 0.8092 pm/Pa. It was important to note variations in the range and step of the measurements taken.

To prepare the sensor for ocean use, where the density differs from fresh water, simulations were conducted. These simulations aimed to anticipate the shift in Bragg wavelength and sensor sensitivity in two distinct fluids, fresh water with a density of (Webb, 2019) and seawater with a density of (Romeo, Albo, and Lago, 2021).

Figure 7 to Figure **10** showed the comparison of simulation results for both types of fluids at temperatures of 4°C, 15°C, 25°C, and 50°C. The chosen temperatures in the simulations aimed to represent the conditions of deep-sea waters in Indonesia. This range covered normal seawater conditions at a depth of 2000 m, which was approximately 4°C (Odumodu and Mode, 2016), to seawater conditions influenced by underwater volcanic activities, reaching temperatures well above 50°C.

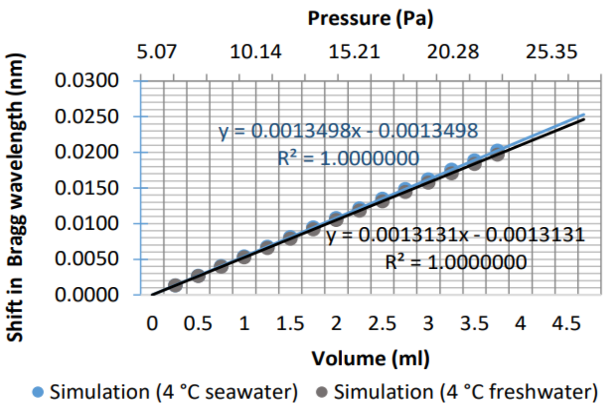

Figure 7 The comparison of simulations between freshwater and seawater at 4°C was made

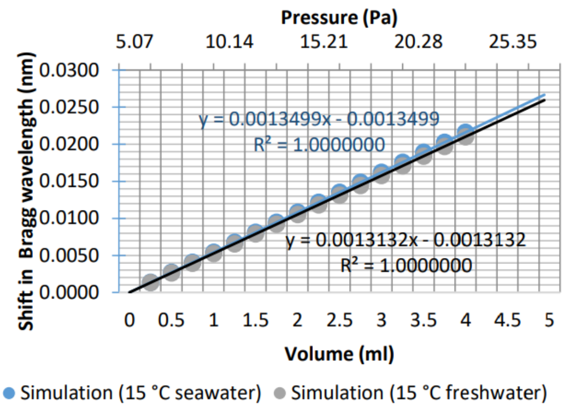

Figure 8 The comparison of simulations between freshwater and seawater at 15°C was made

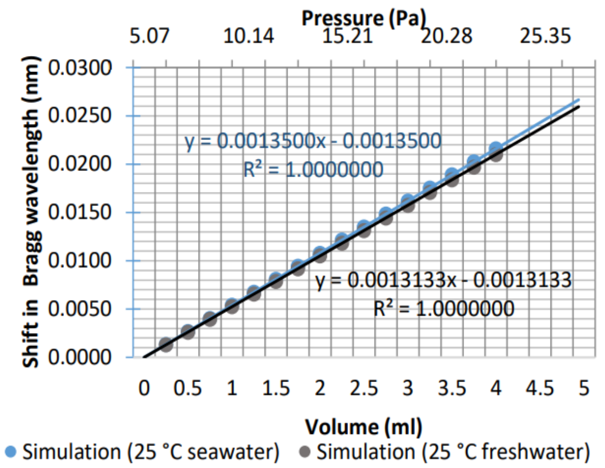

Figure 9 The comparison of simulations between freshwater and seawater at 25°C was done

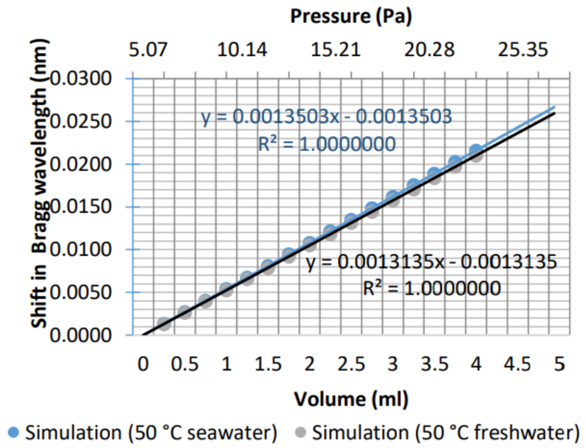

Figure 10 The comparison of simulations between freshwater and seawater at 50°C was done

The simulation results from Figure 7 to Figure **10** showed that as the temperature rose, there was a noticeable increase in the reflected wavelength shift. This increase was more prominently evident in the Table below.

Table 1 Reflected central wavelength shift at various temperature

T (°C)	freshwater (pm)	seawater (pm)
4	1.3131	1.3498
15	1.3132	1.3499
25	1.3133	1.3500
50	1.3135	1.3503

* for every 0.25 ml increase

Using the data provided in the table above, the average increase in the reflected central wavelength shift was nm/0.25 ml or nm/Pa for every 1°C increase in freshwater. In seawater, this increase was nm/0.25 ml or nm/Pa for every 1°C rise.

5. Conclusions

In conclusion, from the laboratory-scale experiment and subsequent data analysis, several key results were obtained. For example, in low hydrostatic pressure measurements using FBG, a threshold of 5.07 Pa with a resolution of 1.69 Pa was established. The results showed a linear relationship between low hydrostatic pressure and the reflected wavelength in the range of 0.75 ml – 4 ml, equivalent to 5.07 Pa - 27.3 Pa hydrostatic pressures. Consequently, the observed sensitivity was 0.8092 pm/Pa, associating with the theoretical basis, and a 4.6% margin of error. Simulations also showed that with an increase in temperature, there was a noticeable increment in the reflected wavelength shift. On average, there was an increase of 5.22898×10^{-9} nm/Pa for each 1°C increment in freshwater and 5.3754×10^{-9} nm/Pa for each 1°C increment in seawater.

Acknowledgments

The authors are grateful to the Faculty of Engineering, University of Indonesia, 2022-2023 for providing support through the Seed Funding Grant No: NKB-1957/UN2.F4.D/ PPM.00.00/2022 and RIIM Grant 2022-02 (G3) No: RIIM-30141557602.

References

Amos, S., Prabhu, R., Nuguna, J., 2017. Theoretical Design and Analysis of a Sensing System for High Pressure and Temperature Measurement in Subsea Underwater Applications. *In:* OCEANS 2017 - Aberdeen

Bhowmik, K., Peng, G-D., Luo, Y., Ambikairajah, E., Lovric, V., Walsh, W.R., Rajan, G., 2015. Experimental Study and Analysis of Hydrostatic Pressure Sensitivity of Polymer Fibre Bragg Gratings. *Journal of Lightwave Technology*, Volume 33, pp. 2456–2462

Dwiyantoro, A., Nugraha, I., Choi, D., 2016. A Simple Hierarchical Activity Recognition System Using a Gravity Sensor and Accelerometer on a Smartphone. *International Journal of Technology*, Volume 7(5), pp. 831–839

Her, S-C. Weng, S-Z., 2021. Fiber Bragg Grating Pressure Sensor Integrated with Epoxy Diaphragm. *Sensors*, Volume 21(9), p. 3199

Irfan, M., Haryadi, Y., Haryanto, D., Rusdiansyah, A., 2021. Tinjauan Teknis Penempatan Sistem Mooring Buoy dan OBU INA-TEWS di Dasar Laut *(Technical Review of the Placement Mooring Buoy System and OBU Ina-TEWS on the Seabed)*. *Oseanika: Jurnal Riset dan Rekayasa Kelautan*, Volume 2(1), pp. 1–16

Kumar, H., Sharan, A., and Sreerangaraju, M.N., 2021. Underwater Acoustic Pressure Sensing using Optical Fiber Bragg Grating. *In:* 8th International Conference on Computing for Sustainable Global Development (INDIACom), New Delhi

Leal-Junior, A.G., Díaz, C.A.R., Frizera, A., Marques, C., Ribeiro, M.R.N., Pontes, M.J., 2019. Simultaneous Measurement of Pressure and Temperature With a Single FBG Embedded in a Polymer Diaphragm. *Optics and Laser Technology*, Volume 112, pp. 77–84

Lei, X., 2020. Underwater Pressure and Temperature Sensor Based on a Special Dual-Mode Optical Fiber. *IEEE Access*, Volume 8, pp. 146463–146471

Matsumoto, H., Kimura, T., Nishida, S., Machida, Y., Araki, E., 2018. Experimental Evidence Characterizing Pressure Fluctuations at the Seafloor-Water Interface Induced by an Earthquake. *Scientific Reports*, Volume 8(1), p. 16406

Nguyen, V.Q., Chiang, C.-C., Tsai, L., 2022. Enhanced Sensitivity of Bare FBG Pressure Sensor Based on Oval-Shaped 3D Printed Structure. *Optical Fiber Technology*, Volume 73, p. 103022

Nishida, S., Machida, Y., Araki, E., Kawaguchi, K., 2018. Level Adjustor of Mobile Pressure Calibrator for Ocean Bottom Pressure Gauge. *In:* OCEANS - MTS/IEEE Kobe Techno-Oceans (OTO)

Odumodu, C.F.R., Mode, A.W., 2016. Geothermal Gradients and Heat Flow Variations in Partsof the Eastern Niger Delta, Nigeria. *Journal of the Geological Society of India*, Volume 88(1), pp. 107–118

Ramirez, J.P., Stefanini, C., Masi, G.D., Romano, D., 2022. Design of Magnetic Coupling-Based Anti-Biofouling Mechanism for Underwater Optical Sensors. *Computer Science,* p. arXiv:2201.12015

Romeo, R., Albo, P.G., Lago, S., 2021. Density and Derived Properties of Standard Seawater up to High Pressure in Stable and Metastable States. *Deep Sea Research Part I: Oceanographic Research Papers* , Volume 177, p. 103624

Rong, Q., Qiao, X., 2019. FBG for Oil and Gas Exploration. *Journal of Lightwave Technology*, Volume 37(11), pp. 2502–2515

Singh, M.J., Choudhary, S., Chen, W-B., Wu, P-C., Goyal, M.K., Rajput, A., Borana, L., 2023. Applications of Fibre Bragg Grating Sensors for Monitoring Geotechnical Structures: A Comprehensive Review. *Measurement*, Volume 218, p. 113171

Suastika, K., Sahlan., Nugroho, W.H., Zubaydi, A., Misbah, M.N., Murdjito, 2019. Fatigue Life Assessment of Waste Steel Reused as Tsunami Buoy Keel Structures: A Case Study. *International Journal of Technology*, Volume 10(4), pp. 700–709

Tanguy, A., Li, Y., Mengxi, T., 2021. Research on Testing Methods of Temperature Strain and Force Strain under Extreme Temperature Environment. *In:* International Conference on Innovative Solutions in Hydropower and Environmental and Civil Engineering December 11-13 2020, Beijing, China

Tanioka, Y., 2018. Tsunami Simulation Method Assimilating Ocean Bottom Pressure Data Near a Tsunami Source Region. *Pure and Applied Geophysics*, Volume 175, pp. 721–729

Webb, P., 2019. *Introduction to Oceanography.* Rebus Community, Minneapolis

Werneck, M., Allil, R., Nazare, F., 2017. *Fiber Bragg Gratings: Theory Fabrication, and Applications.* SPIE Press Book

Winarno, Sutejo, B., Febriawan, H.K., Idham, H., Widiaputra, T., Pianto, T.A., Avianti, ,E., Anatoly, N., 2021. Buoy Monitoring System in Lombok Strait for The Indonesian Tsunami Coastal Acoustic Tomography (Ina-CAT). *In:* IEEE Ocean Engineering Technology and Innovation Conference

Yang, M., Zhu, Y., An, R., 2022. Temperature and Pressure Sensor Based on Polished Fiber-Optic Microcavity. *IEEE Photonics Technology Letters*, Volume 34(11), pp. 607–610

Yang, Y., Hong, C., Abro, Z.A., Wang, L., Yifan, Z., 2019. A New Fiber Bragg Grating Sensor Based Circumferential Strain Sensor Fabricated Using 3D Printing Method. *Sensors and Actuators A: Physical*, Volume 295, pp. 663–670

Zainudin, M., Sulaiman, M.N., Mustapha, N., Perumal, T., Mohamed, R., 2017. Recognizing Complex Human Activities using Hybrid Feature Selections based on an Accelerometer Sensor. *International Journal of Technology*, Volume 8(5), pp. 968–978

Zhang, Y., Zhang, W., Zhang, Y., Chen, L., Yan, T., Wang, S., Yu, L., Li, Y., 2017. 2-D Medium–High Frequency Fiber Bragg Gratings Accelerometer. *IEEE Sensors Journal*, Volume 17(3), pp. 614–618

Zhang, Y.-j., Tian, Y.-s., Fu, X.-h., 2017. Wide-Range Fiber Bragg Grating Displacement Sensor with Temperature Compensation. *In:* 2nd International Conference for Fibre-optic and Photonic Sensors for Industrial and Safety Applications (OFSIS)